Asn^{494} to Gln^{494} and Asn^{636} to Gln^{636}. This mutant shows similar affinity for LDL as compared to the wild-type extracellular domain [with the use of a plate-binding assay similar to (*15*)]. Secreted carboxyl-terminally His-tagged protein was purified by Ni affinity chromatography [in 25 mM sodium phosphate (pH = 8) and 500 mM NaCl, eluted with 500 mM imidazole], Mono Q [25 mM sodium phosphate (pH = 8) and 100 mM NaCl, eluted with NaCl], and gel filtration on a Superdex-200 column [25 mM sodium phosphate (pH = 8), 150 mM NaCl] and then crystallized out of precipitate (space group $P3_121$) with 50 mM sodium acetate (pH = 5.3), 3% 1,2 hexanediol, and 0.5 mM $CaCl_2$. The crystals contained one molecule in the asymmetric unit and 74% solvent. Micromolar amounts of sodium 12-tungstophosphate were soaked into crystals to prepare for the multiwavelength anomalous diffraction (MAD) experiment. The crystals cracked upon soaking and were radiation sensitive, so hundreds had to be screened for isomorphous pieces suitable for data collection under cryogenic conditions.

29. The structure was determined with MAD techniques. Diffraction data were collected at Advanced Light Source (ALS) (5.0.2 and 8.2.1) and Advanced Photon Source (APS) (ID-19). The data were processed with MOSFLM (*42*) and SCALA (*43*) or HKL2000 (*44*), followed by programs from the CCP4 suite (*43*) and SHARP (*45*) for the structure determination. Data collected at the peak, inflection, and high-energy remote wavelengths have high merging statistics as a consequence of the large anomalous signal. This was confirmed by analyzing non-Bijvoet merged data as well as by data collected at the low-energy remote wavelength. The cluster sites were derived from anomalous difference Pattersons with the use of peak data and confirmed by anomalous difference Fourier techniques with the use of molecular replacement phases obtained from the correctly positioned model pdb:1IJQ (*5*) done by CNS (*46*). The tungsten positions in the cluster were modeled on the basis of the small molecule structure (*47*). Experimental density–modified phases (with no model contribution or data sharpening) provided an electron density sufficient to fit the polypeptide trace for each module unambiguously. All the modules of the extracellular domain are visible except for R1 amino-terminal sequencing of the protein from crystals shows that the first residue is Asp^4, suggesting that while R1 is present it is disordered. As a starting point for model-building, we used the fragments from PDB 1AJJ, 1D2J, 1I0U, and 1IJQ. Including the model in the phase calculation and sharpening the data by applying a resolution-dependent B factor [exp ($-B/d^2$), where d is the resolution and $B = -120$ Å^2, derived from the Wilson plot of the data] resolved many of the side chains. The model includes amino acids 44 to 693, except Arg^{57}, Val^{58}, Asp^{75}, Lys^{99}, Cys^{100} to Ser^{102}, Val^{388}, Val^{441}, Gln^{453}, and Ala^{454}, for which there is poor density because of heavy atom Fourier ripples from the clusters. About 10% of the residues are currently modeled as alanines. For molecular surface calculations, all side chains were incorporated. Restrained positional refinement with a maximum likelihood target function including experimental phase information was applied with CNS to regularize the model. Crystallographic refinement is problematic because of the poor ratio of observations to parameters (with 17,303 unique reflections and more than 5000 atoms) and the lack of noncrystallographic symmetry. The R_{work} is 38.8% with the use of all reflections $F > 0$ between 33.1 and 3.7 Å; the R_{free} is 39.2%, calculated with a test set of 7% of the total reflections. The model has root mean square (rms) bond-length deviations of 0.03 Å and 4.9° for bond angles. The model has 583 residues in the most favored and allowed regions and 58 in the generous region, whereas six residues are currently in the unfavorable regions of the Ramachandran plot [PROCHECK (*43*)]. Figures were made with CLUSTAL W (*48*), MOLSCRIPT (*49*), RASTER 3D (*50*), and GRASP (*51*).
30. G. Rudenko *et al.*, unpublished data.
31. D. R. Van der Westhuyzen *et al.*, *Biochem. J.* **277**, 677 (1991).
32. T. Clackson, J. A. Wells, *Science* **267**, 383 (1995).
33. T. Doi *et al.*, *J. Biol. Chem.* **269**, 25598 (1994).
34. S. Wragg, K. Drickamer, *J. Biol. Chem.* **274**, 35400 (1999).
35. S. G. Young, *Circulation* **82**, 1574 (1990).
36. X. Wang, R. Pease, J. Bertinato, R. W. Milne, *Arterioscler. Thromb. Vasc. Biol.* **20**, 1301 (2000).
37. V. Raussens, C. M. Slupsky, R. O. Ryan, B. D. Sykes, *J. Biol. Chem.* **277**, 29172 (2002).
38. J. E. Chatterton *et al.*, *J. Lipid Res.* **36**, 2027 (1995).
39. S. Keidar, A. C. Goldberg, K. Cook, J. Bateman, G. Schonfeld, *J. Lipid Res.* **30**, 1131 (1989).
40. J. R. McNamara, D. M. Small, Z. Li, E. J. Schaefer, *J. Lipid Res.* **37**, 1924 (1996).
41. Y. Toyota, T. Yamamura, Y. Miyake, A. Yamamoto, *Atherosclerosis* **147**, 77 (1999).
42. A. G. W. Leslie, *Joint CCP4 and ESF-EACBM Newsletter on Protein Crystallography* (Science and Engineering Research Council Daresbury Laboratory, Warrington, UK, 1992), issue 26.
43. Collaborative Computational Project Number 4, *Acta Crystallogr.* **D 50**, 760 (1994).
44. Z. Otwinowski, W. Minor, *Methods Enzymol.* **276**, 307 (1997).
45. E. de la Fortelle, G. Bricogne, *Methods Enzymol.* **276**, 472 (1997).
46. A.T. Brunger *et al.*, *Acta Crystallogr.* **D 54**, 905 (1988).
47. J.-C. P. Gabriel, R. Nagarajan, S. Natarajan, A. K. Cheetham, C. N. R. Rao, *J. Solid State Chem.* **129**, 257 (1997).
48. J. D. Thompson, D. G. Higgins, T. J. Gibson, *Nucleic Acids Res.* **22**, 4673 (1994).
49. P. J. Kraulis, *J. Appl. Crystallogr.* **24**, 946 (1991).
50. E. A. Merritt, D. J. Bacon, *Methods Enzymol.* **277**, 505 (1997).
51. A. Nicholls, K. Sharp, B. Honig, *Proteins* **11**, 281 (1991).
52. Single-letter abbreviations for the amino acid residues are as follows: A, Ala; C, Cys; D, Asp; E, Glu; F, Phe; G, Gly; H, His; I, Ile; K, Lys; L, Leu; M, Met; N, Asn; P, Pro; Q, Gln; R, Arg; S, Ser; T, Thr; V, Val; W, Trp; Y, Tyr; and X, any amino acid.
53. We thank the staff at the synchrotrons APS ID-19 and ALS 5.0.2 and 8.2.1 for excellent support, Y. Chelliah for initial studies on the insect cell overexpression system, M. Machius and R. Sunahara for crucial discussions, and T. C. Südhof and M. Machius for reviewing the manuscript. J.L.G. and M.S.B. acknowledge the support of grants from the NIH (HL20948) and the Perot Family Foundation. The atomic coordinates have been deposited to the Protein Data Bank, accession code 1N7D.

5 September 2002; accepted 15 November 2002
Published online 28 November 2002;
10.1126/science.1078124
Include this information when citing this paper.

REPORTS

Formation of a One-Dimensional Array of Oxygen in a Microporous Metal-Organic Solid

Ryo Kitaura,[1] Susumu Kitagawa,[1]* Yoshiki Kubota,[2] Tatsuo C. Kobayashi,[3] Koichi Kindo,[3] Yoshimi Mita,[4] Akira Matsuo,[3] Michihiro Kobayashi,[4] Ho-Chol Chang,[1] Tadashi C. Ozawa,[3] Megumi Suzuki,[4] Makoto Sakata,[5] Masaki Takata[5,6]

We report the direct observation of dioxygen molecules physisorbed in the nanochannels of a microporous copper coordination polymer by the MEM (maximum entropy method)/Rietveld method, using in situ high-resolution synchrotron x-ray powder diffraction measurements. The obtained MEM electron density revealed that van der Waals dimers of physisorbed O_2 locate in the middle of nanochannels and form a one-dimensional ladder structure aligned to the host channel structure. The observed O–O stretching Raman band and magnetic susceptibilities are characteristic of the confined O_2 molecules in one-dimensional nanochannels of CPL-1 (coordination polymer 1 with pillared layer structure).

The confinement of molecules into low-dimensional nanospace may alter their properties and reactivity, especially in the case of O_2 molecules, which have rich redox and magnetic properties arising from their unpaired electrons (*1*, *2*). In spite of many experimental and theoretical investigations, the adsorption mechanism and ordering state of adsorbed O_2 molecules that form a specific array in nanochannels are not yet clear (*3*, *4*). In the past decade, various novel nanochannel structures constructed with metal-organic frameworks have been produced and studied with regard to their adsorption performance with various gas molecules (*5*–*8*). If the gas molecules could be trapped in mid-channel, low-dimensional nanostructures could be designed, depending on the host channel structure.

Our strategy to elucidate the specific structure of O_2 molecules adsorbed in nanochannels uses a crystalline microporous copper coordination polymer that forms a uniform nanosized one-dimensional (1D) channel. We obtained accurate powder x-ray diffraction (XRD) data by synchrotron powder diffraction with a large Debye-Scherrer camera and were able to image the diffraction data by the MEM (maximum entropy method)/Rietveld method, which enabled us to determine a precise electron density map (*9*–*12*).

The 3D structure of the porous Cu(II) coordination polymer, which we determined previously with single-crystal diffraction data (*13*), is shown in Fig. 1. A 2D sheet constructed by Cu(II) and pzdc (2,3-pyrazinedicarboxylate) were linked by pyz (pyrazine) to form a pillared layer structure, which we call CPL-1 (coordination polymer 1 with pillared layer structure). 1D channels with dimensions of 4.0 Å by 6.0 Å formed between the 2D sheets along the *a* axis, with one water molecule being included per Cu(II) ion.

In order to adsorb O_2 molecules into the nanochannels, we heated CPL-1 under reduced pressure to remove water molecules from the channels, and then dosed CPL-1 with O_2 gas while cooling. The in situ powder XRD patterns of as-synthesized CPL-1 and of anhydrous CPL-1 with O_2 at 80 kPa over the temperature range from 300 to 90 K are shown in Fig. 2. The changes can be categorized into three stages: (i) after heating under reduced pressure to remove water molecules; (ii) during the cooling process, between 130 and 150 K; and (iii) after the reheating process from 90 to 300 K. No change was observed in the absence of O_2 over the full temperature range. LeBail fitting of the powder diffraction data of Fig. 2 revealed a cell volume contraction at (i), expansion at (ii), and recontraction at (iii). We attribute these changes to structure distortion arising from framework flexibility, which is triggered by (i) desorption of water molecules and then the (ii) adsorption and (iii) desorption of O_2 molecules (*14*).

The crystal structure of anhydrous CPL-1 at 120 K without O_2 molecules determined by Rietveld analysis of the powder data up to 53.3° ($d > 0.89$ Å) reveals that the porous structure was identical to that of as-synthesized CPL-1, with only slight structure distortions (*15*). The MEM electron density distribution map of the anhydrous CPL-1 (Fig. 3A), whose reliability factor based on structure factors, R_F, is 1.6%, shows that no water molecules exist in the nanochannel (*16*, *17*).

The space group of the anhydrous CPL-1 with O_2 at a pressure of 80 kPa at 90 K (Fig. 2G) is assigned as the same space group, $P2_1/c$, as CPL-1 without O_2. The cell parameters were determined as a = 4.68759(4) Å, b = 20.4373(2) Å, c = 10.9484(1) Å, and β = 96.9480(6)° by Rietveld analysis. As the preliminary model, we used the same structure model corresponding to Fig. 3A for CPL-1 without O_2, in the pre-Rietveld analysis for the MEM/Rietveld analysis. The reliability factors based on the powder pattern, R_{wp}, and the integrated intensities, R_I, were 18.5 and 54.2%, respectively. However, the MEM electron density visualized the O_2 density feature in the middle of the nanochannel.

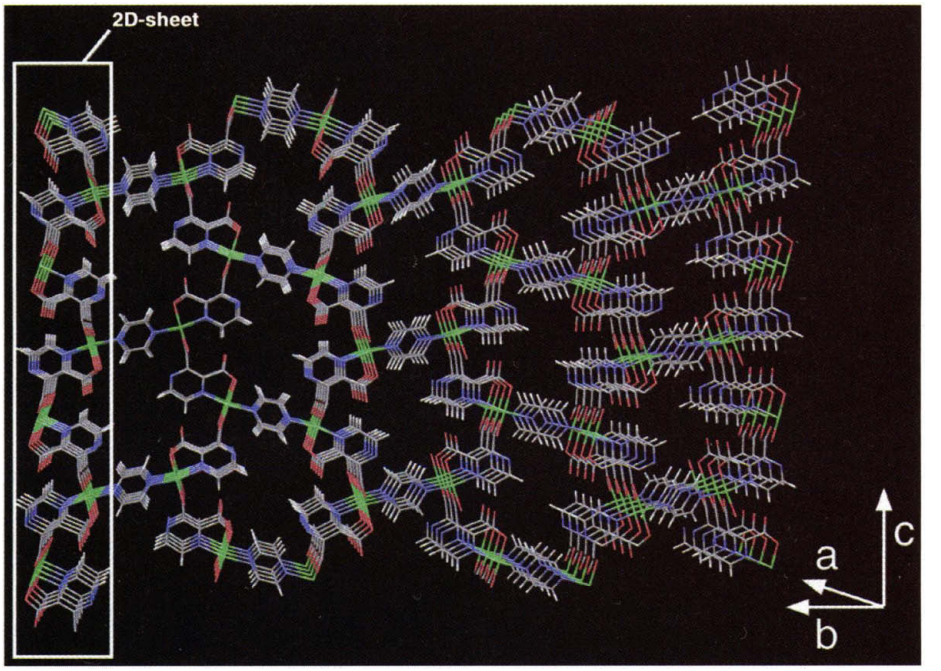

Fig. 1. Representation of the 3D porous pillared layer structure of CPL-1 down from the *a* axis (Cu, green; O, red; C, gray; N, blue). Water molecules are omitted for clarity. Crystal data were as follows: $C_{16}H_{12}Cu_2N_6O_{10}$, M = 575.40, monoclinic, space group $P2_1/c$ (no. 14), a = 4.693(3) Å, b = 19.849(2) Å, c = 11.096(2) Å, β = 96.90(2)°, V = 1026.1(6) Å^3, Z = 2, R_1 = 0.062, and R_w = 0.062. The elemental analysis calculated for $C_{16}H_{12}Cu_2N_6O_{10}$ was as follows: C, 33.40%; H, 2.10%; and N, 14.61%. The amounts found were: C, 32.78%; H, 1.57%; and N, 14.34%.

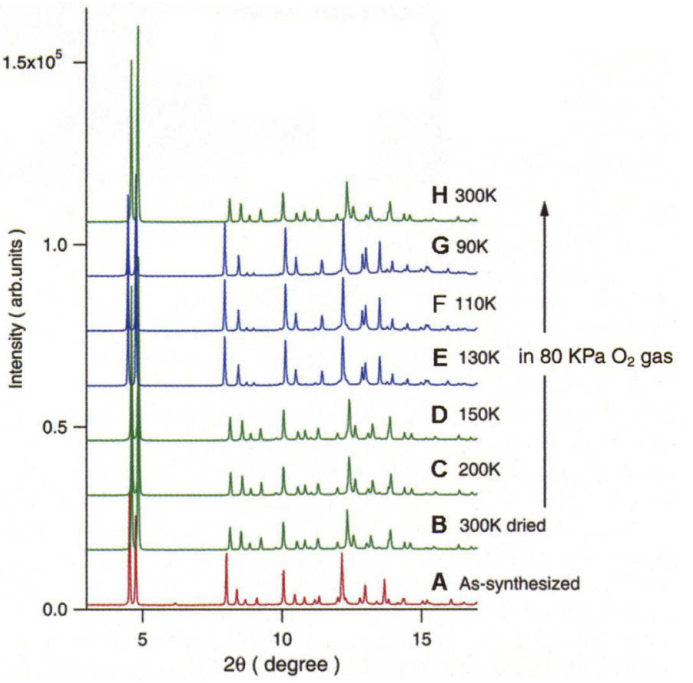

Fig. 2. Synchrotron XRD patters of (**A**) as-synthesized CPL-1 at 300 K and anhydrous CPL-1 (after drying at 373 K under reduced pressure) with O_2 of 600 torr with cooling from 300 to 90 K and reheating to 300 K. (**B** to **H**) represent XRPD patterns at 300, 200, 150, 130, 110, 90, and 300 K, respectively.

[1]Department of Synthetic Chemistry and Biological Chemistry, Graduate School of Engineering, Kyoto University, Yoshida, Sakyo-ku, Kyoto 606–8501, Japan. [2]Department of Environmental Sciences, Osaka Women's University, Sakai, Osaka 590–0035, Japan. [3]KYOKUGEN, [4]Department of Physical Science, Graduate School of Engineering Science, Osaka University, Toyonaka, Osaka, 560–8531, Japan. [5]Department of Applied Physics, Nagoya University, Nagoya 464–8603, Japan. [6]JASRI/Spring-8, Koto, Hyougo, 679–5189, Japan.

*To whom correspondence should be addressed. E-mail: Kitagawa@sbchem.kyoto-u.ac.jp

After a revision based on the electron density, the Rietveld refinement dramatically improved, and the R_{wp} and R_I of the final Rietveld fitting became 2.1 and 3.9%, respectively. The final electron densities, obtained by MEM whose reliability factor, R_F, was 1.5%, reveal the 3D pillared-layer structure, consistent with the single-crystal data (Fig. 3B).

The peanut-shaped electron densities, which are presumably due to O_2 molecules, are clearly recognized in the middle of the channels. There is a total of 15.8(1) electrons, calculated on the basis of the MEM results, which virtually agrees with the number in the O_2 molecule. Therefore, we deduced that the interlayer peanut-shaped electron densities are O_2 molecules, and one O_2 molecule was adsorbed per copper atom without any electron transfer between O_2 molecules and/or O_2 molecules and the pore wall.

The O_2 adsorption isotherm measured at 77 K shows a type I isotherm with a saturated amount of adsorption of 1.0 O_2 molecules per copper atom, which is in good agreement with the MEM/Rietveld analysis. The relatively small value of the isotropic displacement parameter [B = 4.1(2) Å^2] and lack of disorder of O_2 molecules indicate that O_2 molecules adsorbed in the nanochannels resemble the solid state rather than the liquid state at 90 K, which is much higher than the freezing point of O_2 under atmospheric pressure, 54.4 K (*18*). This freezing behavior should be attributed to the strong confinement effect of the nanochannel. The overall crystal structure and geometry of O_2 molecules, based on the above analysis, are represented in Fig. 4. Two O_2 molecules align parallel to each other along the *a* axis with an inclination of 11.8°, and the intermolecular distance is 3.28(4) Å, which is much smaller than the minimum of the Lennard-Jones potential of R_e = 3.9 Å (*19*). This intermolecular distance is close to the nearest distance in solid α-O_2, which is stable below 24 K. This result indicates that O_2 molecules adsorbed in nanochannels form van der Waals dimers, $(O_2)_2$, and their successful structural characterization has now been reported. Each dimer aligns along the *a* axis to form a 1D ladderlike structure. The interatomic distance of oxygen atoms in the adsorbed O_2 molecule was found to be 1.245(50) Å.

In order to investigate the properties of adsorbed O_2 molecules, magnetic susceptibilities and Raman spectroscopic measurement were performed. The susceptibility for adsorbed O_2 molecules, which is the difference in those between CPL-1 with O_2 and CPL-1 without O_2, approaches zero with decreasing temperature, indicating a nonmagnetic ground state (Fig. 5). Correspondingly, in the high-field magnetization process, the difference between CPL-1 with and without O_2 can be observed above 50 T (Fig. 5, inset). The magnetization process of CPL-1 is a paramagnetic curve with a saturated moment of 1 bohr magneton for a Cu atom, which can be expected for the usual magnetic Cu ion. The CPL-1 with O_2 shows a small difference in the low-field region but a steep increase above 50 T, indicating a magnetic transition from the nonmagnetic to the magnetic state. This magnetization process can be understood as a behavior of the antiferromagnetic dimer or the 1D antiferromagnetic chain with bond alternation. On the basis of structural information about the adsorbed O_2 molecule in CPL-1, the nonmagnetic ground state is associated with the antiferromagnetic dimer. The antiferromagnetic interaction ($\mathcal{H} = -2J\mathbf{S}_1\mathbf{S}_2$) is estimated as $J/k_B \sim -50$ K, which is larger than that of the α phase of $J/k_B \sim -30$ K (*20*). Figure 6 shows Raman spectra of CPL-1 around 90 K with and without O_2 molecules. A sharp peak due to the stretching mode of adsorbed O_2 molecules is observed at 1561 cm^{-1}, which is slightly higher than that of liquid or solid oxygen at ambient pressure

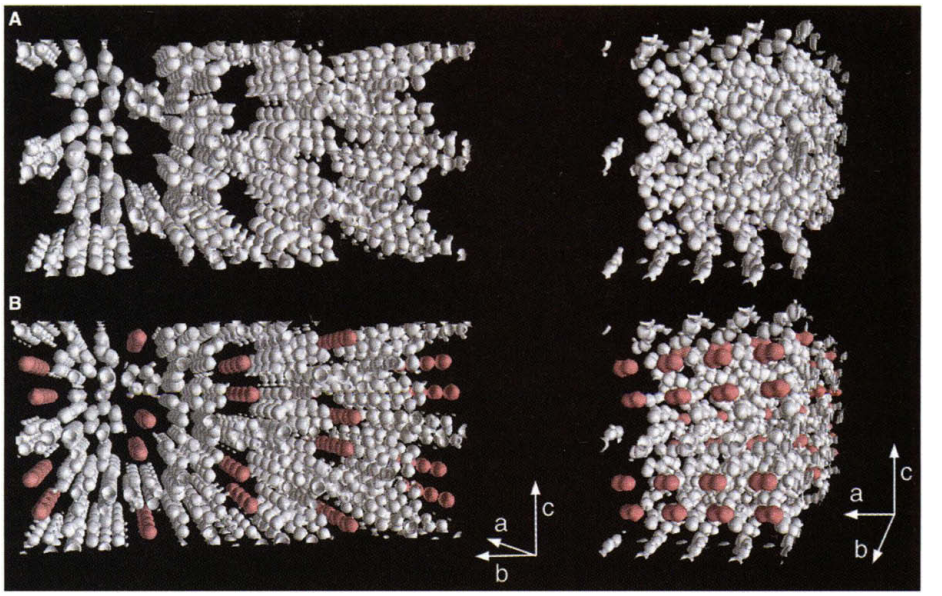

Fig. 3. MEM electron densities of (**A**) anhydrous CPL-1 without O_2 molecules at 120 K and (**B**) CPL-1 with adsorbed O_2 at 90 K as an equal-density contour surface. The equicontour level is 1.0 e Å^{-3}.

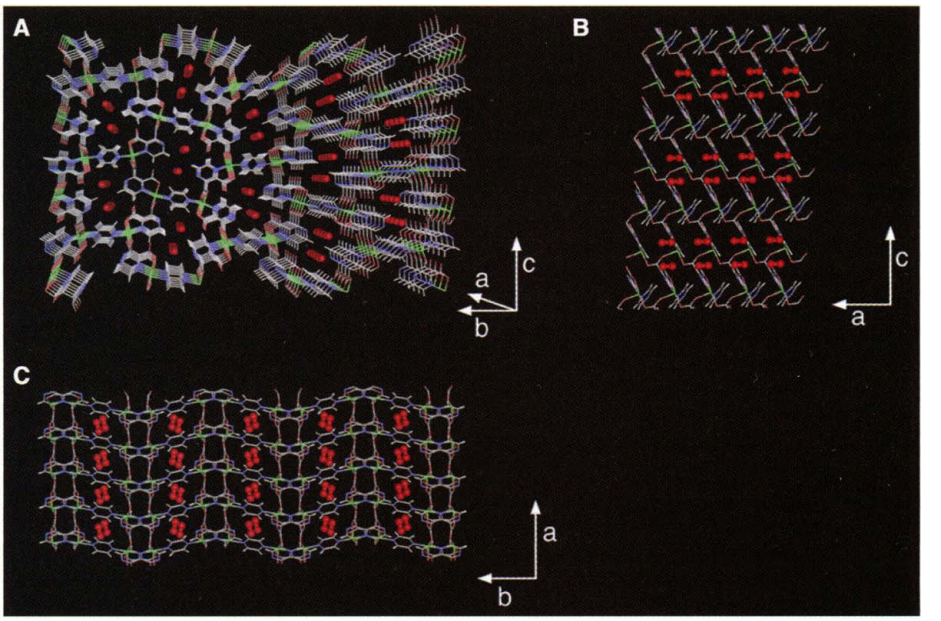

Fig. 4. Schematic representation of CPL-1 with adsorbed O_2 at 90 K. (**A**) The perspective view down from the *a* axis. (**B**) and (**C**) Views down from the *b* axis and *c* axis, respectively.

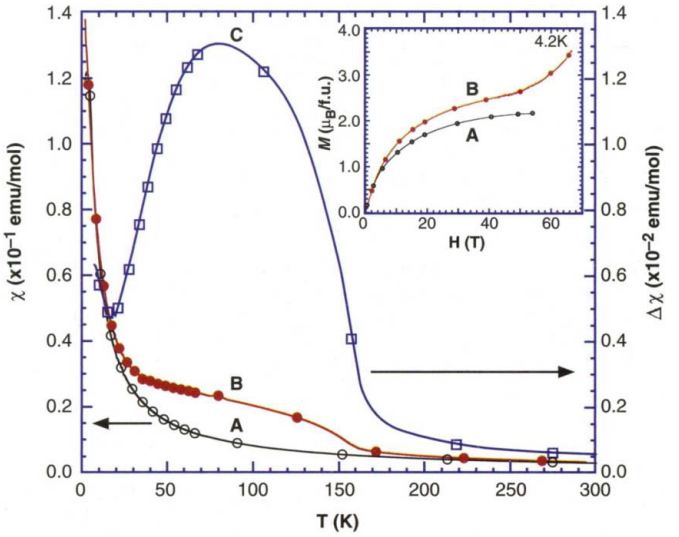

Fig. 5. Temperature dependence of the susceptibility of (**A**) CPL-1 and (**B**) CPL-1 with O_2 molecules, and (**C**) the differences between (A) and (B), correspond to the contribution from adsorbed O_2 molecules. (Inset) High-field magnetization process of (A) CPL-1 and (B) with O_2 molecules. χ, susceptibility; M, magnetization; μ_B, bohr magneton; f.u., formula unit; H, magnetic field T, temperature.

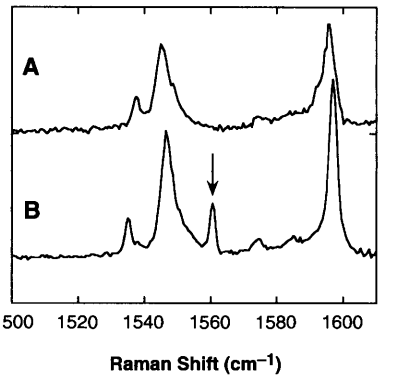

Fig. 6. Raman spectra of (**A**) CPL-1 and (**B**) CPL-1 with O_2 molecules. A peak due to the stretching of O_2 molecules (marked by an arrow) is shown in (B). The abscissas were calibrated using the standard lines from a neon lamp, and the resolution of the data is 0.6 cm^{-1}.

(*21*), comparable with that of α phase at a pressure of 2 GPa.

The confinement effect and the restricted geometry resulting from 1D nanochannels of CPL-1 lead to a specific molecular assembly: a 1D ladder structure constructed of O_2 dimers, which is unlikely to be bulk fluid and/or solid.

References and Notes

1. W. Mori *et al.*, *Mol. Cryst. Liq. Cryst.* **306**, 1 (1997).
2. U. Köbler, R. Marx, *Phys. Rev. B* **35**, 9809 (1987).
3. H. Kanoh, A. Zamma, N. Setoyama, Y. Hanzawa, K. Kaneko, *Langmuir* **13**, 1047 (1997).
4. W. A. Steele, *Langmuir* **12**, 145 (1996).
5. M. Eddaoudi *et al.*, *Acc. Chem. Res.* **34**, 319 (2001).
6. B. Moulton, M. J. Zaworotko, *Chem. Rev.* **101**, 1629 (2001).
7. S. Noro, S. Kitagawa, M. Kondo, K. Seki, *Angew. Chem. Int. Ed. Engl.* **39**, 2082 (2000).
8. K. Seki, *Chem. Commun.* **16**, 1496 (2001).
9. M. Takata, E. Nishibori, M. Sakata, *Z. Kristallogr.* **216**, 71 (2001).
10. M. Takata *et al.*, *Nature* **377**, 46 (1995).
11. C.-R. Wang *et al.*, *Nature* **408**, 426 (2000).
12. E. Nishibori *et al.*, *J. Phys. Chem. Solids* **62**, 2095 (2001).
13. M. Kondo *et al.*, *Angew. Chem. Int. Ed. Engl.* **38**, 140 (1999).
14. R. Kitaura, K. Fujimoto, S. Noro, M. Kondo, S. Kitagawa, *Angew. Chem. Int. Ed. Engl.* **41**, 133 (2002).
15. The space group was assigned as $P2_1/c$, and the lattice parameters were determined by Rietveld analysis as follows, a = 4.71534(6) Å, b = 19.8280(2) Å, c = 10.7184(1) Å, and β = 95.1031(10)°. R_{wp} and R_I were 2.6 and 3.3%, respectively.
16. The MEM analysis was carried out by the computer program ENIGMA. The unit cell was divided into pixels (128 by 512 by 256) in calculation.
17. H. Tanaka *et al.*, *J. Appl. Crystallogr.* **35**, 282 (2002).
18. M. Miyahara, K. E. Gubbins, *J. Chem. Phys.* **106**, 2865 (1997).
19. J. O. Hirschfelder, C. F. Curtiss, R. B. Bird, *Molecular Theory of Gases and Liquids* (Wiley, New York, 1954).
20. C. Ueda, K. Sugiyama, M. Date, *J. Phys. Soc. Jpn.* **54**, 1107 (1985).
21. K. Bier, H. Jodl, *J. Chem. Phys.* **81**, 1192 (1984).

22. The synchrotron radiation experiments were performed at the Spring-8 with the approval of the Japan Synchrotron Radiation Research Institute (JASRI). We thank H. Tanaka for the computer program ENIGMA for the MEM analysis, K. Kato for his experimental help at Spring-8, and K. Miura for providing adsorption measurement apparatus. Supported by a grant-in-aid for Scientific Research from the Ministry of Education, Culture, Science, Sports and Technology of Japan.

16 September 2002; accepted 13 November 2002

Structure-Assigned Optical Spectra of Single-Walled Carbon Nanotubes

Sergei M. Bachilo,[1] Michael S. Strano,[1] Carter Kittrell,[1] Robert H. Hauge,[1] Richard E. Smalley,[1,2] R. Bruce Weisman[1]*

Spectrofluorimetric measurements on single-walled carbon nanotubes (SWNTs) isolated in aqueous surfactant suspensions have revealed distinct electronic absorption and emission transitions for more than 30 different semiconducting nanotube species. By combining these fluorimetric results with resonance Raman data, each optical transition has been mapped to a specific (*n*,*m*) nanotube structure. Optical spectroscopy can thereby be used to rapidly determine the detailed composition of bulk SWNT samples, providing distributions in both tube diameter and chiral angle. The measured transition frequencies differ substantially from simple theoretical predictions. These deviations may reflect combinations of trigonal warping and excitonic effects.

Many of the major challenges currently facing basic and applied research on SWNTs arise from the diversity of tube diameters and chiral angles in samples formed through any preparative method. Because the electronic and optical properties of nanotubes vary substantially with structure (*1*), these samples show mixed characteristics that hinder basic investigations and limit some of the most promising applications. The recent discovery of band-gap fluorescence from semiconducting SWNTs in aqueous micelle-like suspensions (*2*) opens the door to powerful experimental approaches that can extract the spectroscopic properties of specific tube structures through bulk measurements. We report such a spectrofluorimetric study, in which distinct first and second van Hove optical transitions are measured for 33 different nanotube species and then assigned to specific structures. Our findings provide a tool for analyzing the detailed composition of bulk nanotube samples, one that can be adapted to monitor and guide processes aimed at separating tubes by type.

Figure 1A illustrates how each SWNT structure is indexed by two integers (*n*,*m*) that

[1]Department of Chemistry, Center for Nanoscale Science and Technology, and Center for Biological and Environmental Nanotechnology, Rice University, 6100 Main Street, Houston, TX 77005, USA. [2]Department of Physics, Rice University, 6100 Main Street, Houston, TX 77005, USA.

*To whom correspondence should be addressed. E-mail: weisman@rice.edu